Volume 14 | Number 6 | 14 February 2018 | Pages 865–1070

Soft Matter

rsc.li/soft-matter-journal

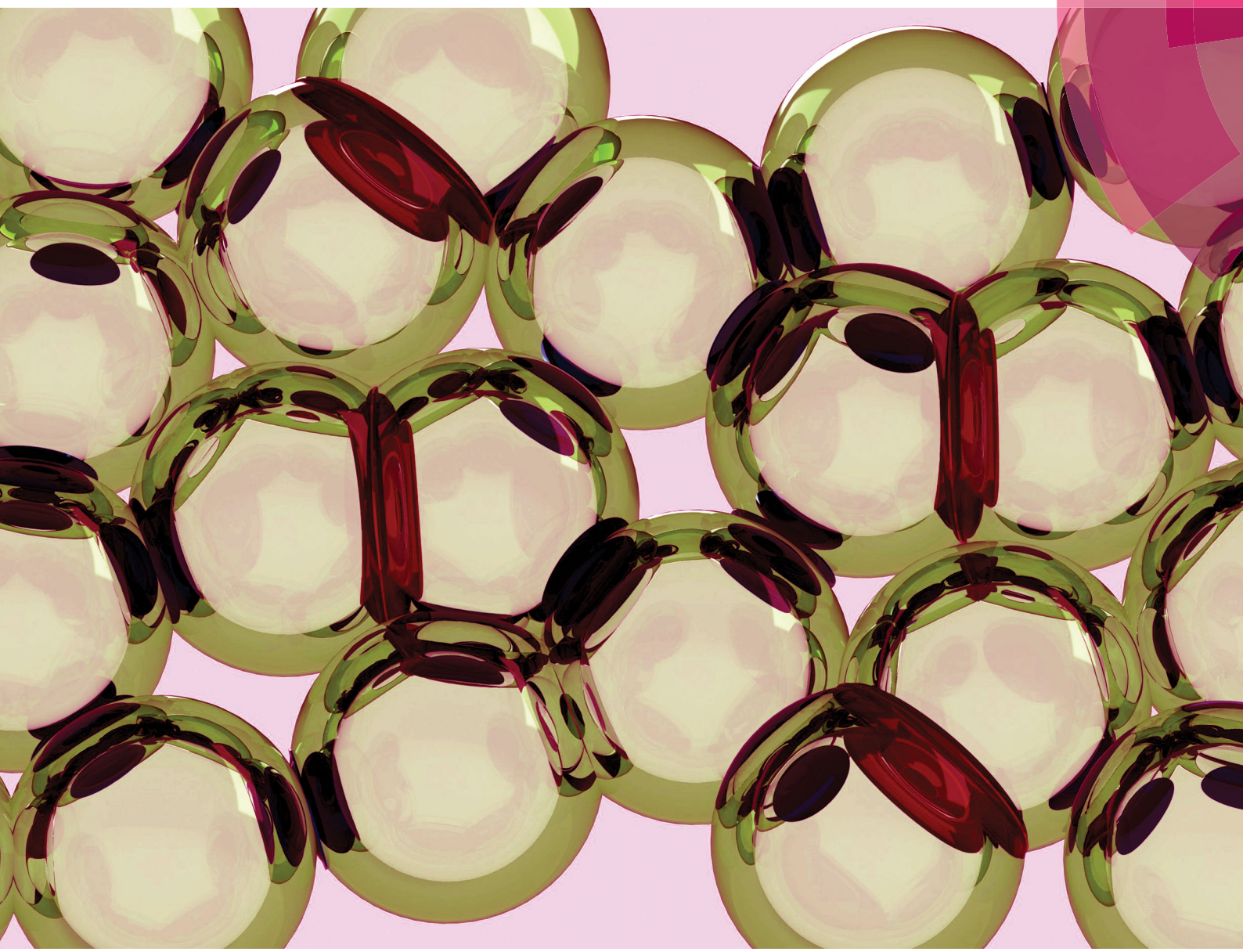

ISSN 1744-6848

ROYAL SOCIETY OF CHEMISTRY

PAPER
Annie Colin *et al.*
Shear thinning in non-Brownian suspensions

Soft Matter

PAPER

Cite this: *Soft Matter*, 2018, **14**, 879

Shear thinning in non-Brownian suspensions

Guillaume Chatté,[a] Jean Comtet,[b] Antoine Niguès,[b] Lydéric Bocquet,[b] Alessandro Siria,[b] Guylaine Ducouret,[a] François Lequeux,[a] Nicolas Lenoir,[cd] Guillaume Ovarlez[e] and Annie Colin *[af]

Received 30th September 2017,
Accepted 26th November 2017

DOI: 10.1039/c7sm01963g

rsc.li/soft-matter-journal

We study the flow of suspensions of non-Brownian particles dispersed into a Newtonian solvent. Combining capillary rheometry and conventional rheometry, we evidence a succession of two shear thinning regimes separated by a shear thickening one. Through X-ray radiography measurements, we show that during each of those regimes, the flow remains homogeneous and does not involve particle migration. Using a quartz-tuning fork based atomic force microscope, we measure the repulsive force profile and the microscopic friction coefficient μ between two particles immersed into the solvent, as a function of normal load. Coupling measurements from those three techniques, we propose that (1) the first shear-thinning regime at low shear rates occurs for a lubricated rheology and can be interpreted as a decrease of the effective volume fraction under increasing particle pressures, due to short-ranged repulsive forces and (2) the second shear thinning regime after the shear-thickening transition occurs for a frictional rheology and can be interpreted as stemming from a decrease of the microscopic friction coefficient at large normal load.

1 Introduction

Suspensions are made of solid particles immersed in a liquid. Their flows are ubiquitous in nature and industry: water or oil saturated sediments, muds, crystal-bearing magma, concrete, silica suspensions, cornflour mixtures, latex suspensions and clays are example of dispersions we meet in our everyday life. Despite the numerous studies performed since Einstein's pioneering work in 1905,[1,2] their rheological properties remain poorly understood.

Let us consider the simple case of an assembly of hard spheres suspended in a fluid of viscosity η_f sheared with shear rate $\dot{\gamma}$, under a constant particle pressure P^p. In the absence of external force scales coming from inertia or thermal forces, these dispersions have to be Newtonian. Indeed, in these systems, there is only one single control parameter, $I_V = \frac{\eta_f \dot{\gamma}}{P^p}$, governing the dynamics of the flow. Following the approaches used in the studies of granular material,[3] the shear stress τ and the solid fraction ϕ are given by two constitutive equations: $\tau = \mu_{eff}(I_V)P^p$ and $\phi = \phi(I_V)$, where $\mu_{eff}(I_V)$ is an effective frictional coefficient. These relations led to $\tau = g(\phi)\eta_f\dot{\gamma}$. In the situation of a homogeneous controlled solid fraction dispersion, solid particles immersed in a Newtonian fluid are viscous. Both shear stress and normal stress differences are proportional to the shear rate. Strikingly, this analysis does not describe the reality. Dispersions exhibit a wide range of rheological behavior including shear thinning and shear thickening.

Shear thickening corresponds to an increase of the viscosity as a function of the shear rate. This behavior is one of the most striking phenomena occurring in complex fluids. In cornflour suspensions, the formation of a dynamic jamming front under impact makes the fluid so resistant that a person can run on it.[4,5] Industrially, shear thickening can have disastrous effects by enhancing the amount of energy required to pump suspensions at high shear rates, damaging mixer blades or clogging pipes.[6] Shear thinning corresponds to a decrease of the viscosity as a function of the shear rate. These non-linear phenomena are essential from the perspective of applications and materials, and a better understanding of controlling the flow of dispersions in industrial processes is required.

At this stage, a global picture describing the mechanisms at the origin of shear thickening starts to emerge. In the absence of inertia, recent theoretical studies have put forward the role of contact forces.[7,8] At low pressure, the particles do not touch. The suspension is a Newtonian fluid. At high pressure,

[a] *ESPCI Paris, PSL Research University, Sciences et Ingénierie de la Matière Molle, CNRS UMR 7615, 10 rue Vauquelin, F-75231 Paris Cedex 05, France. E-mail: annie.colin@espci.fr*
[b] *Laboratoire de Physique Statistique, Ecole Normale Supérieure, UMR CNRS 8550, PSL Research University, 24 rue Lhomond, 75005 Paris Cedex 05, France*
[c] *PLACAMAT, UMS 3626-CNRS/Université de Bordeaux, 33608 Pessac, France*
[d] *Grenoble-INP/UJF-Grenoble 1/CNRS UMR 5521, Laboratoire 3SR, Grenoble, France*
[e] *Univ. Bordeaux, CNRS, Solvay, LOF, UMR 5258, F-33608 Pessac, France*
[f] *Université de Bordeaux, Centre de Recherche Paul Pascal, UPR-8641 CNRS, 115 avenue Schweitzer, 33600 Pessac, France*

repulsive forces are overcome, and frictional contacts are the norm. Depending upon the value of the solid fraction, different behaviors are predicted at high shear rates. At low solid fraction, a gradually denser frictional contact network is observed when the shear rate is increased. This regime corresponds to continuous shear thickening (CST). For higher values of solid fraction ϕ, the theoretical flow curve displays an S-shape allowing discontinuous shear thickening (DST) between a lower (sparse contact network) and an upper (dense contact network) branch at equal strain rates. Both branches correspond to a Newtonian behavior. Finally, for very high solid fraction, the system transits from a liquid state to a solid state unable to flow without fracture. This situation corresponds to shear jamming or shear-induced jamming. This picture and the role of frictional forces have been validated through direct experimental measurements.[9,10] The pairwise force profile and the frictional interactions between pairs of particles have been measured using quartz-tuning fork based atomic force microscopy. The normal load required to transit from lubricated to frictional interactions is quantitatively related to the critical shear stress at the shear thickening transition as predicted by numerical simulations.

Many studies report shear thinning for various suspensions: PMMA particles in polyethylene glycol (PEG),[11] fumed silica particles in polypropylene glycol (PPG),[12] cornstarch particles in water,[13] glass spheres in mineral oil,[14] cementitious pastes,[15] polystyrene particles dispersed in PEG[16] and also PVC particles dispersed in a plasticizer.[17–20]

For Brownian suspensions, shear thinning occurs due to a competition between diffusion and convection. At low shear rates, particle diffusion is significant and particles occupy a larger effective volume than at high shear rates, leading to a larger viscosity. Explanations concerning shear thinning in non-Brownian suspensions are more vague. At low shear rates, in a non-Brownian suspension, shear thinning may occur due to the presence of short-ranged stabilizing repulsive forces between particles. In this situation, the apparent size of the particles includes the hard sphere contribution and a part of the surrounding soft repulsive potential. The apparent size value will decrease with increasing shear rate. Indeed, higher shear rates correspond to higher pressures and thus to a decrease of the minimum possible distance between particles as they flow. The apparent size of the particles and thus the suspension viscosity would then decrease as a function of the shear rate. Such thinning has already been observed in a charge stabilized suspension[21,22] and predicted numerically.[23]

At high shear rates, few other mechanisms have been proposed. Using cornflour suspensions, Ovarlez and coworkers[13] showed that the flow at high shear rates after DST is inhomogeneous. The system separates into two phases: a dilute phase and a concentrated phase. This separation is concomitent with a shear thinning behavior. The shear thinning variation seems to be due to the particular rheological properties of the two shear-induced phases and the evolution of their respective size under shear. However, this explanation may not be universal, as some dispersions display shear thinning by flowing homogeneously. Inspired by the old order–disorder theory of Hoffman *et al.*,[17] Nakajima *et al.*[24] explained the shear thinning at high shear rates by the breakdown of spanning clusters to smaller sizes, releasing the trapped plasticizer and increasing the maximum packing density; thus causing a decrease of viscosity at high shear rates. More recently, elastohydrodynamic interactions have been proposed to explain the shear thinning behavior.[11,25] Under high normal load and shear rates, the particles may deform *via* a lubricating liquid film opposing contact between particles. Last but not least, Vazquez-Queseda[26] and coworkers have proposed recently that shear thinning might be related to the non-Newtonian properties of the solvent. They point out that hidden shear-thinning effects of the suspending medium, which occur at shear rates at orders of magnitude larger than the range investigated experimentally in dispersions, lead to significant shear thinning of the overall suspension at much smaller shear rates. They consider the behavior of the solvent at ultra-high shear rates by assuming that the shear rate in the film between the particles might be much greater than the applied one.

In this article, we revisit the question of shear thinning in non-Brownian suspensions. We take advantage of a system of particles previously characterized. Our subject of study is the dispersion of polyvinyl chloride (PVC) particles suspended in a Newtonian plasticizer (Dinch) (see Fig. 1). This dispersion is an assembly of lubricated grains that becomes frictional at a high shear rate.[9] Using capillary rheometry, X-ray radiography and quartz-tuning fork based atomic force microscopy, we characterize the system in the shear thinning regimes in DST materials. We restrict our study to moderate solid volume fraction values to avoid the shear jamming zone. The main originality of our work is to couple these techniques to get a comprehensive picture of the flow. The first part of the article deals with the description of the sample. We report the rheological study in the second part. The third part is devoted to X-ray radiography analysis. In the fourth part, we report measurements of the solid friction coefficient between two PVC beads in the

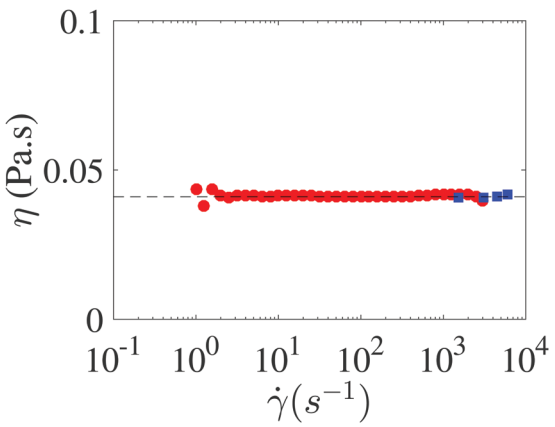

Fig. 1 Flow curve of the liquid Dinch at room temperature (25 °C). Red circles correspond to measurements in a Couette cell (rotational rheometry), whereas blue squares are measurements from a capillary rheometer. The black dotted line stands for 0.041 Pa s.

Newtonian plasticizer at high shear rate. The fifth part deals with discussion and outlook.

2 Materials under scrutiny

The dispersions under scrutiny are PVC particles dispersed in liquid 1,2-cyclohexane dicarboxylic acid di-isononyl ester (Dinch). We prepare our dispersions by weighing a given amount of PVC particles and a given amount of Dinch. The continuous phase is Newtonian up to 10^4 s^{-1} and has a viscosity of 41 mPa s at room temperature (*cf.* Fig. 1). There is no observable thinning in the whole range of shear rates investigated, which rules out the mechanism proposed in ref. 26 for our suspensions. This oil does not evaporate, which allows for long experiments. The solid fractions are then calculated knowing the density of PVC ρ_{PVC} = 1.38 g cm^{-3} and the density of Dinch ρ_d = 0.95 g cm^{-3}. The solid volume fraction used in this study is $\phi = \frac{m_{PVC}/\rho_{PVC}}{m_{PVC}/\rho_{PVC} + m_d/\rho_d}$ where m_{PVC} is the mass of PVC particles and m_d is the mass of Dinch. Dinch is an organic solvent that acts as a plasticizer for the particles. Dinch enters the particles, creates a polymer brush around them and eventually completely swells them. Above the glass transition temperature of PVC (T_g = 80 °C), this process occurs in less than one minute. However, at room temperature, this process is far slower and takes more than one year. Thus, Dinch swells only the particle surface of a few nanometers (experimentally measured in ref. 9) at room temperature creating a swelled PVC brush layer at the particle surface that sterically stabilizes our suspensions.[27] The dispersions are used for a maximum of two days after preparation to avoid variation of the interactions between particles (ageing). Suspensions are also degassed prior to experiments. In this work, we focus on concentrated non-Brownian suspensions. The solid fraction varies between 50% and 64%.

We focus on two dispersions of PVC particles. SEM images of the particles are displayed in Fig. 2 while particle size distributions in Dinch are displayed in Fig. 3. In the first dispersion (D1), the mean particle radius, defined as $R_{32} = \langle R^3\rangle/\langle R^2\rangle$, is 1 μm. The size distribution is lognormal and the standard deviation estimated using the volume distribution is 45%. In the second dispersion (D2), the particle size histogram using a volume distribution is trimodal with lognormal peaks around 350 nm (with a standard deviation of 25%), 3.3 μm (with a standard deviation of 55%) and 20 μm (with a standard deviation of 22%). Both dispersions will reach Peclet numbers ($\mathrm{Pe} = \frac{6\pi\eta_s R^3\dot{\gamma}}{k_B T} \sim 250\dot{\gamma}$ where η_f is the suspending fluid viscosity, $\dot{\gamma}$ is the shear rate and R is the particle radius) in the range of 10–10^6 for which Brownian effects are practically negligible.[28]

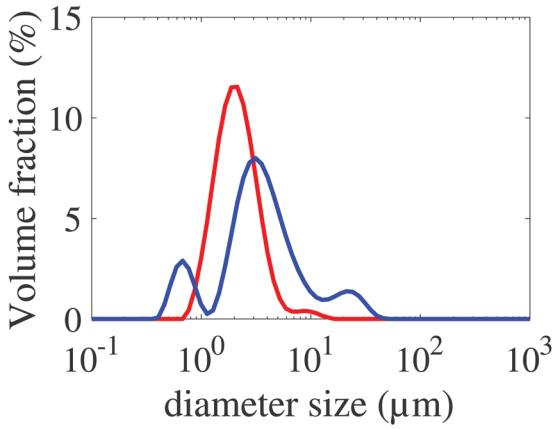

Fig. 3 Particle size distributions of D1 (red) and D2 (blue) obtained with a laser diffraction apparatus (Mastersizer 3000 from Malvern).

The random close packing fractions ϕ_{RCP} of these dispersions are measured. ϕ_{RCP} corresponds to the value of the solid fraction at which the viscosity diverges at low shear rate under the hypothesis of frictionless particles.[9] We measure the value of the viscosity at $\dot{\gamma}$ = 10 s^{-1} to get rid of interparticle interactions at low shear rate.[29] The data are fitted using a Krieger–Dougherty model $\eta = \eta_s\left(1 - \frac{\phi}{\phi_{RCP}}\right)^{-n}$, where η_s is the solvent viscosity. We get ϕ_{RCP} = 69.4% ± 0.25% for D1 suspensions and

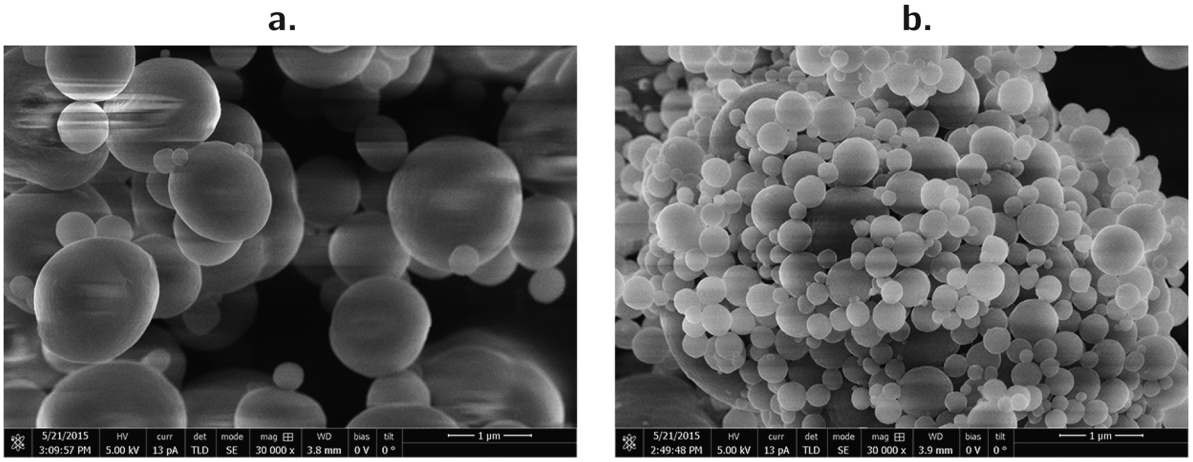

Fig. 2 Scanning Electron Microscopy (SEM) images of (a) PVC used for D1 and (b) PVC used for D2. Scale bar at the bottom right of each image is 1 μm.

ϕ_{RCP} = 77.2% ± 0.25% for D2 suspensions. The exponents n of the Krieger–Dougherty models are respectively n = 2.3 for the D1 dispersion and n = 2.9 for the D2 dispersion. η_s is equal to 41 mPa s.

3 Rheology

3.1 Experimental set-up

To measure the rheological properties over a large range of shear rate, we combined measurements from both rotational and capillary rheometers. For normal stress differences lower than 1000 Pa, global rheological measurements were performed on a stress-controlled rheometer (DHR-3 from TA instruments) or on a strain-controlled rheometer (ARES from TA Instruments). We used either a Couette cell (gap e = 1 mm, inner radius R_1 = 14 mm, and height H = 42 mm) with smooth surfaces or a cone-and-plate geometry with smooth surfaces of diameter 25 mm (angle $\alpha = 2^\circ$). The temperature was fixed at 25 °C. The geometry of the Couette rheometer is a conventional cup and bob with a conical bottom. The truncation is equal to 2 mm. The rheometer measures (or imposes depending upon the controlled mode) both the torque Γ exerted on the geometry and its angular velocity Ω in real-time. From Ω and Γ, a global shear rate $\dot{\gamma}$ and a global shear stress σ were computed as a function of time.

This computation resulted from the assumption that (i) the flow is azimuthal (*i.e.* the flow field is purely tangential), (ii) the fluid is Newtonian and does not slip at the wall. Under these assumptions, $\dot{\gamma}$ and σ are simply proportional to ω and Γ, respectively, with proportionality factors that depend upon the geometrical parameters of the shear cell. For a Couette cell, these links write:

$$\dot{\gamma} = \frac{R_1^2 + R_2^2}{R_2^2 - R_1^2}\Omega \quad (1)$$

$$\sigma = \frac{R_1^2 + R_2^2}{4\pi H R_1^2 R_2^2}\Gamma \quad (2)$$

where R_1 and R_2 are respectively the inner radius and the external radius of the Couette geometry and H is the height of the Couette cell. In a cone-and-plate cell, we get:

$$\dot{\gamma} = \frac{\Omega}{\tan(\alpha)} \quad (3)$$

$$\sigma = \frac{3\Gamma}{2\pi R^3} \quad (4)$$

where R is the radius of the cone–plate and α is the angle of the cone–plate.

As discussed earlier, we use two procedures: an applied shear rate procedure and an applied shear stress procedure. For the applied shear stress procedure, we apply the following instructions. At room temperature (25 °C), we first apply a pre-shear step at $\dot{\gamma}$ = 10 s^{-1} for 60 s that allows us to start the experiment with a well-defined steady state. We then apply a ramp of increasing shear stress. The shear stress is swept logarithmically from 1 to 1300 Pa. When two consecutive measurements are within 5%, an equilibrium is assumed and the shear stress is increased. For the applied shear rate procedure, we also apply a pre-shear step at $\dot{\gamma}$ = 10 s^{-1} for 60 s. We then apply a ramp of increasing shear rate. The shear rate is swept logarithmically from 0.1 to 1000 s^{-1}. When two consecutive measurements are within 5%, equilibrium is assumed and the shear rate is increased. We checked the reproducibility of the flow curve measurements using the two procedures. We anticipate that the shear stress procedure allows a better characterization of the rheological properties in the shear thickening transition.

In all cases, the rotational rheometer cannot access normal stress differences N_1 higher than 1000 Pa due to sample ejection or edge instability. This corresponds to the region of the shear thickening transition close to the maximal viscosity measured. We discarded such data. To circumvent these issues at high shear rate and high normal load, we used two kinds of capillary rheometers: a home-made capillary rheometer to access the intermediate range of shear rates and a commercial capillary rheometer (Gottfert Rheo-Tester) to access larger shear rates. This approach has been used previously for PVC particle suspensions in several works.[18–20] The Gottfert Rheo-Tester capillary rheometer is equipped with a capillary die of diameter D = 0.5 mm (silicon carbide; 3 length-to-diameter ratios: L/D = 4, 8, and 16) or with a capillary die of D = 0.3 mm (silicon carbide; 2 length-to-diameter ratios: L/D = 4 and 8). L is the length of the capillary. The volumetric flow rate Q is imposed by imposing to the piston successive steps of increasing speed from 0.1 to 1 mm s^{-1}. The drop of pressure is measured thanks to a pressure transducer of 100 bar (10 MPa) full scale.

Home-made capillary rheometers are displayed in Fig. 4. They consist of a manometer (pressure range 0–8 bars) plugged on a compressed air network (0–7 bars), a syringe with a piston and a capillary firmly plugged to the syringe. Two kinds of syringes are used: (i) commercial ones in plastic with a volume of 30 mL (Fig. 4a). The capillary used is made of PEEK (polyether ether ketone) polymer, which ensures good rigidity. The real die diameter was measured with an optical microscope and found to be 1.55 mm. The capillary length used varies between experiments but is always between 12 and 25 mm. (ii) A home-made syringe made up of PMMA with a larger volume of 250 mL (Fig. 4b). The latter one is nearly transparent to X-ray and will be used in the experiments devoted to the measurement of particle volume fractions. The die diameter is 2.0 mm and different lengths are available (L = 6.5, 11.5 or 16.5 mm). In contrast to the commercial capillary rheometer described earlier, these in-house built capillary rheometers work in a stress-controlled mode. Stress is imposed and computed from air pressure. The shear rate is computed from the flow rate, which is measured by weighing the amount of sample going out from a cup after and before a known time of experiments.

Capillary rheometers measure or impose the drop of pressure ΔP required to get a given flow rate Q. From these data, they compute a shear rate at the wall $\dot{\gamma}_w$ and a shear stress at the wall σ_w. The wall shear stress σ_w is given by:

$$\sigma_w = \frac{\Delta P}{2L/R + l_e} \quad (5)$$

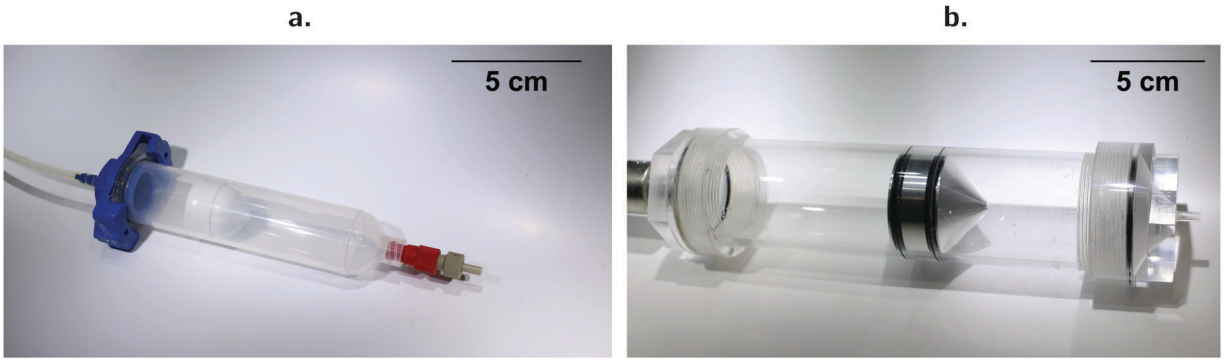

Fig. 4 A home-made device for capillary measurements consisting of a manometer branched on a compressed air network (pressure range 0–8 bars), a syringe with a piston and a capillary at the exit of the syringe. Pressure is imposed and flow rate is measured by weighting. (a) Purchased syringe (V = 30 mL, σ_{max} = 20 kPa); (b) home-made syringe (V = 250 mL, σ_{max} = 50 kPa). The piston is the white part in (a) and the metallic part in (b).

where ΔP is the drop of pressure, L is the length of the die, R is the radius of the die and l_e is an equivalent length of the die representing the extra entrance drop of pressure. It is measured by using Bagley plots[30] that report the drop of pressure ΔP as a function of the L/R ratio for a given flow rate. These plots are lines and l_e corresponds to the intersection of the line with the abscissa (see Fig. 6).

The shear rate at the wall is given by the Weissenberg–Rabinowitsch analysis[31] (Fig. 7):

$$\dot{\gamma}_w = \left(\frac{3n+1}{4}\right)\frac{4Q}{\pi R^3} \quad (6)$$

where $n = \dfrac{\mathrm{dlog}\,\sigma_w}{\mathrm{dlog}\left(\dfrac{4Q}{\pi R^3}\right)}$. The viscosity is then defined as $\eta = \dfrac{\sigma_w}{\dot{\gamma}_w}$. We checked that the resulting flow curves do not depend upon the radius of the capillary tubes, which proves that no slip at the wall is present in our experiments (see the figure). Note that this behavior is not universal. Usually slip at the wall is measured in dispersions. Attractive interactions[32] between the walls and the PVC particles might be at the origin of this phenomenon. The resulting flow curves are plotted in Fig. 5.

3.2 Flow curves

The rheological curves for both samples D1 and D2 are reported in Fig. 5. Subfigures (a) and (c) display the rheological response for D1 suspensions with solid fractions equal to ϕ = 55% (open symbols) and ϕ = 60% (filled symbols). Subfigures (b) and (d) display the rheological response for D2 suspensions with solid fractions ϕ = 60% (open symbols) and ϕ = 64% (filled symbols). All the dispersions share a common behavior. The experimental data collected with various experimental setups collapse on a single flow curve. The dispersions exhibit a slight shear thinning behavior at low shear rate, a shear thickening behavior in the intermediate range of shear rate and a strong shear thinning behavior at high shear rate. D2 dispersions display a continuous shear thickening transition whatever the value of the solid fraction, whereas D1 dispersions display a discontinuous shear thickening transition at high solid fractions. The presence of a shear thinning region beyond the shear thickening region has been reported previously in the literature, but has not been studied in great detail. Let us underline that this behavior is not universal. Newtonian behavior after continuous shear thickening has been observed in PPMA suspensions for a solid fraction of less than 40%, $CaCO_3$ suspensions for a solid fraction of less than 25%, or for charged Brownian polymer spheres (see ref. 25 and the references in ref. 25). However, we are not aware of studies reporting a Newtonian plateau after discontinuous shear thickening. Our data of the viscosity in the high shear rate shear thinning regime can be fitted *versus* shear rate by a power law scaling (linear in log–log graph, *cf.* dotted lines in Fig. 5a and c). All fits have a correlation coefficient over 0.99. The slopes showing viscosity scaling in the shear thinning region at low and high shear rates are plotted in Fig. 8 as a function of the solid fraction divided by the random close packing fraction ϕ_{RCP} of each dispersion in order to ease comparison.

In the low shear rate situation, the exponent does not depend on the dispersion nor on the solid fraction ϕ. It is roughly equal to -0.4. In the high shear rate situation, the exponent of the power law depends upon the volume fraction. The higher the volume fraction, the higher the absolute value of the exponent. Data from D1 and D2 collapse roughly on the same straight line. The point for n close to -0.7 is the only case where the absence of wall slip has not been checked.

Shear thinning with no wall slip is striking for non-Brownian suspensions immersed in a Newtonian fluid. Post-DST shear thinning has been previously associated with shear-induced migration.[13] In order to probe the homogeneity of the flow, we perform X-ray absorption measurements.

4 Particle volume fraction measurements under flow

To measure particle volume fraction under flow, we couple rheometry with *in situ* X-ray radiography. The device used is a phoenix v|tome|x from General Electrics, which is able to do 2D X-ray inspection or 3D computed tomography. Here we use it only in 2D mode by undertaking radiography of spatial X-ray absorption and then monitoring the real-time spatial particle

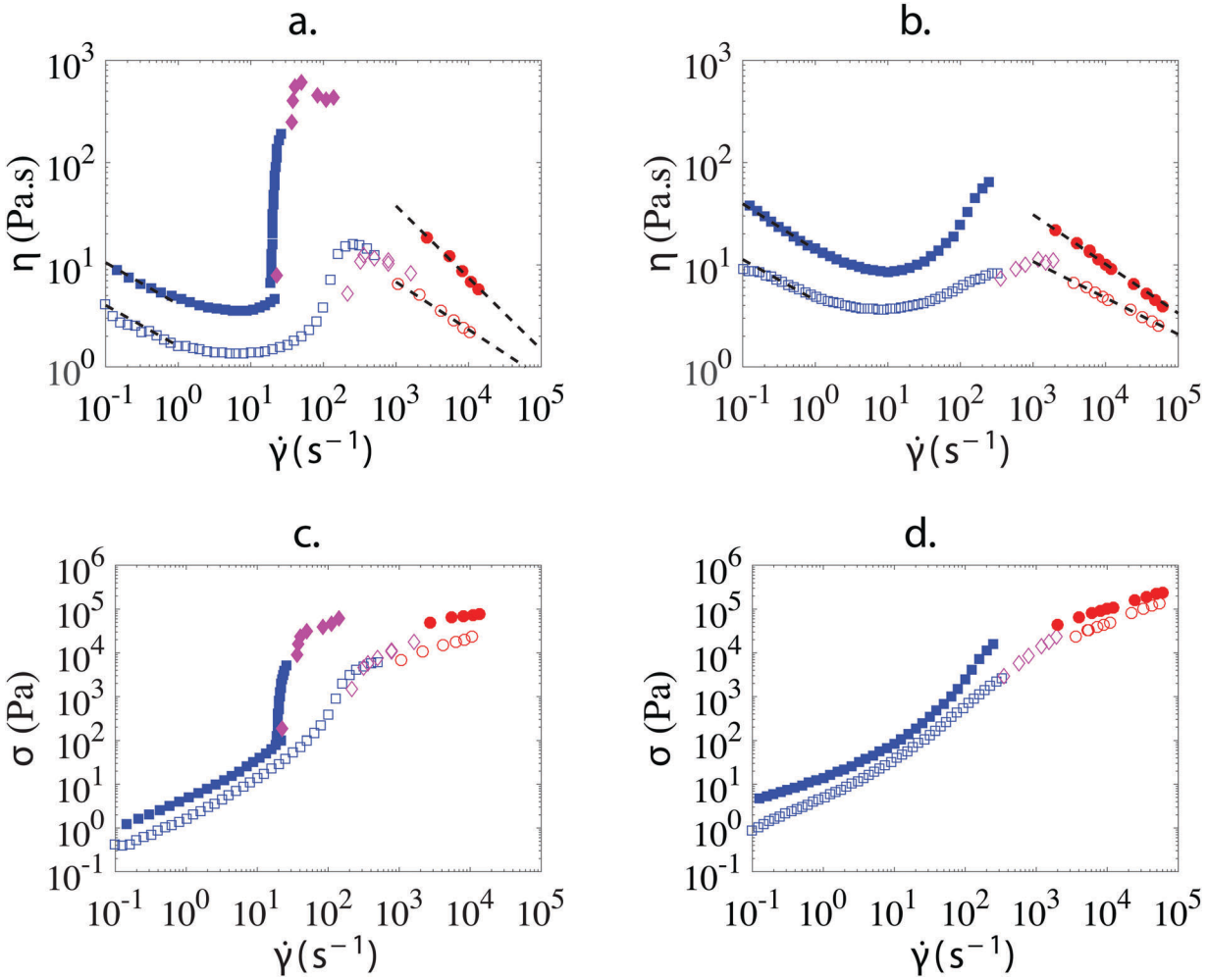

Fig. 5 (a) Flow curves $\eta(\dot{\gamma})$ of D1 55% (open symbols) and 60% (closed symbols); (b) flow curves of D2 60% (open symbols) and 64% (closed symbols); (c) same as (a) but for $\sigma = f(\dot{\gamma})$; (d) same as (a) but for $\sigma = f(\dot{\gamma})$. For all curves, blue squares are obtained from the rotational rheometer; purple diamonds from the in house-built capillary rheometer and red circles from the commercial capillary rheometer. Dotted lines are power law fits of $\eta = g(\dot{\gamma})$.

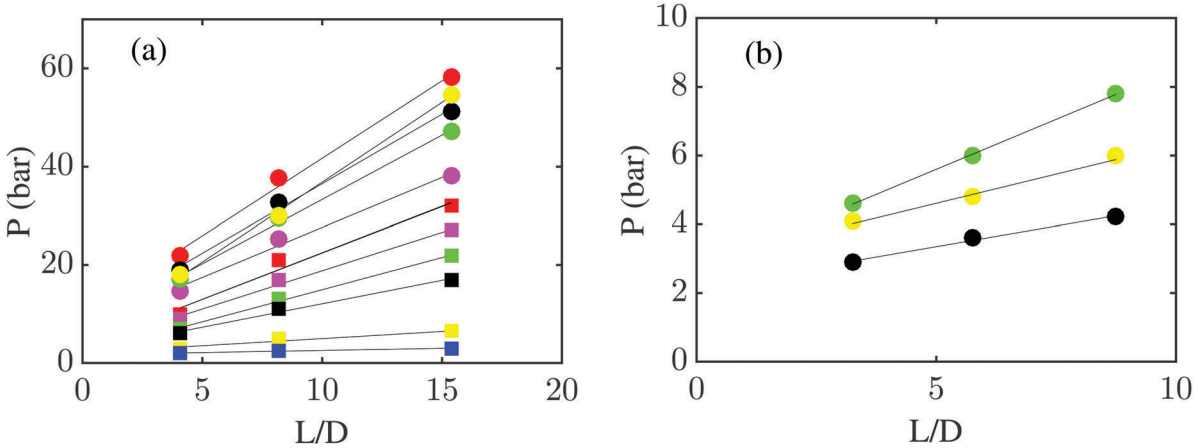

Fig. 6 (a) Bagley plot for the commercial rheometer for D1 (circles) and D2 (squares) at 60%: pressure *versus* L/D for different shear rates: from top to bottom, the shear rates are given by 13 490 s^{-1}, 10 800 s^{-1}, 8100 s^{-1}, 5400 s^{-1}, 2700 s^{-1}, 9258 s^{-1}, 7407 s^{-1}, 5555 s^{-1}, 3703 s^{-1}, 1852 s^{-1}, and 925 s^{-1}. (b) Bagley plot for the home-made rheometer for D1 at 60%: from top to bottom, the shear rates are given by 25 s^{-1}, 33.7 s^{-1}, and 41 s^{-1}. Dotted lines are linear fits. Their intercepts with the y-axis represent the entrance pressure losses for each shear rate.

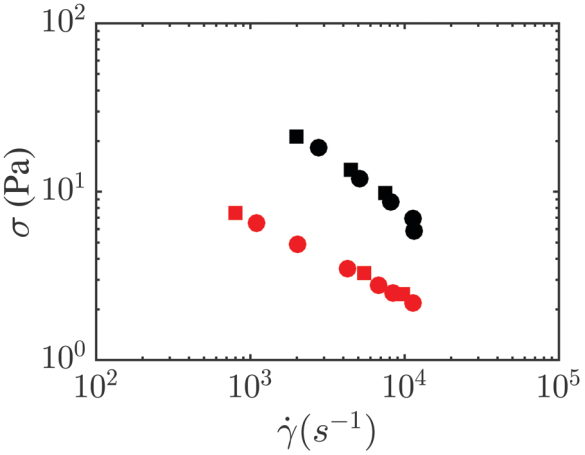

Fig. 7 Rheological curve obtained for D1 (top 60% and bottom 55%). The squares correspond to a file with a diameter of 5 mm, and the circles to a file with a diameter of 3 mm. These measurements suggest no slip at the wall.

repartition upon flow. The apparatus allows us to get 2 pictures per second and thus to probe the evolution of the sample under flow. The experimental set-up and the measurement methods have been described in detail in ref. 33. We recall here the main points.

Fig. 9 is a schematic that shows a planar wave of the X-ray penetrating the syringe. In the experiments, the camera's response is first calibrated to provide a homogeneous intensity response I_0 over all pixels when there are no objects between the X-ray source and the detector. When an object is present, X-rays are absorbed by the various media crossing the beam (the PMMA, the PVC particles, the Dinch, the air) following Beer–Lambert's law. In our situation, the recorded intensity reads:

$$\frac{I(y,z,t)}{I_0} = \exp\left[-L_{\mathrm{syr}}(y,z)\mu_{\mathrm{syr}} - L_{\mathrm{gap}}(y,z)(\Phi(y,z,t)\mu_{\mathrm{b}}(y,z) + (1-\Phi(y,z,t))\mu_{\mathrm{f}}(y,z)\right] \quad (7)$$

where μ_{syr}, μ_{b} and μ_{f} are the attenuation coefficients of respectively the PMMA from the syringe, the PVC beads and the fluid Dinch; and I_0 is the intensity of the planar wave, L_{syr} is the thickness of the PMMA from the syringe and L_{gap} is the thickness of the sample inside the syringe.

This can be read:

$$I(y,z,t) = I_{\mathrm{fluid}}(y,z)\exp(-L_{\mathrm{gap}}(y,z)(\Phi(y,z,t)\mu_{\mathrm{beads}}(y,z) - \mu_{\mathrm{fluid}}(y,z))) \quad (8)$$

where $I_{\mathrm{fluid}}(y,z)$ is the recorded intensity in the absence of particles (liquid Dinch alone).

This leads to:

$$\Phi(y,z,t) = \frac{\ln(I(y,z,t)/I_{\mathrm{fluid}}(y,z))}{\ln(I(y,z,0)/I_{\mathrm{fluid}}(y,z))}\Phi(y,z,0) \quad (9)$$

From the intensity field, eqn (9) allows us to measure the variation (in both time and space) of the averaged particle volume fraction seen by the beam $\Phi(y,z,t)$ in the syringe as a function of the applied drop of pressure. Please note that we did not compute directly the local volume fraction $\phi(y,z,t)$, but only averaged the particle volume fraction seen by the beam along its path through the syringe.

We focus on the suspension exhibiting DST (D1 at ϕ = 60%). More precisely, we are interested in the DST region and the shear thinning observed beyond. We take advantage of our home-made PMMA syringe that enables viscosity measurements both in the DST and the shear thinning beyond. The syringe was placed in the X-ray tomograph. Viscosity measurements were carried out simultaneously with X-ray absorption recording (*cf.* Fig. 9).

From the X-ray radiography data, we extract the value of the solid fractions. These 10 measurements have been performed using a high spatial resolution (less than 20 microns). The noise is 1%. This noise is homogeneously distributed in space and time. Averaging these data leads to a variation of 0.3%. We thus conclude that the sample is homogeneous before, during and after the shear thickening transition. Note that this contrasts with the case of the

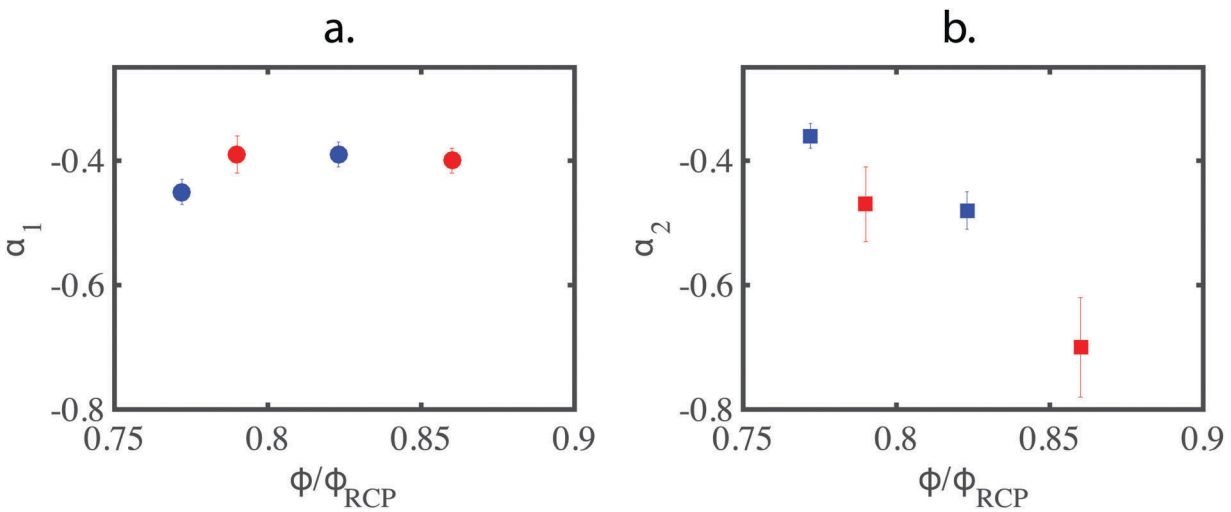

Fig. 8 Slopes (α_1 and α_2) for D1 (red symbols) and D2 (blue symbols) extracted from a power law fit of ($\eta = \dot{\gamma}^{\alpha_1}$) in the first (a) and second ($\eta = \dot{\gamma}^{\alpha_2}$) (b) shear thinning regions (above shear thickening) as measured by the commercial capillary rheometer. To ease comparison between the two PVC powders, solid volume fractions ϕ are normalized by the respective random close packing ϕ_{RCP}.

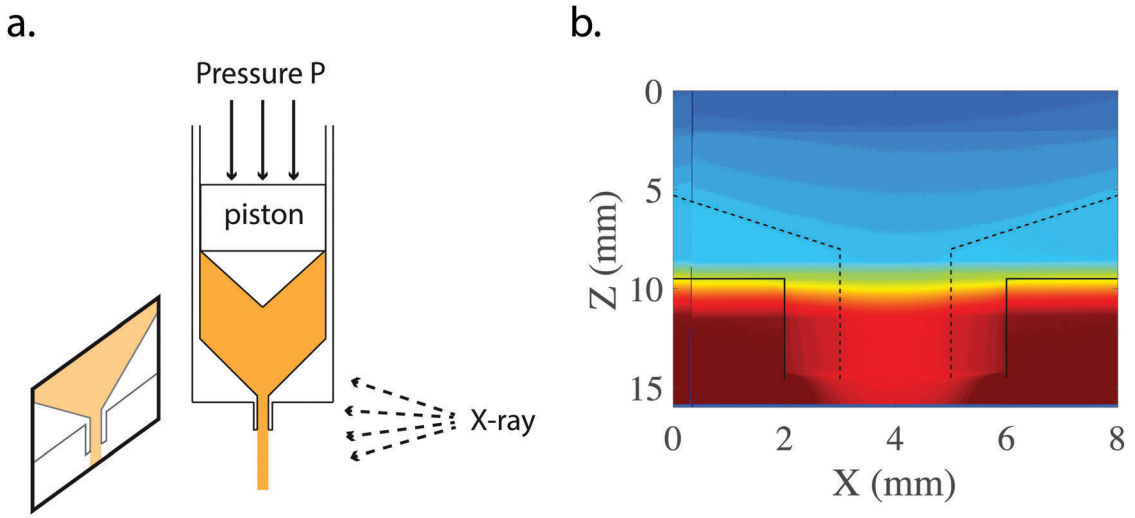

Fig. 9 (a) Scheme of the home-made capillary rheometer placed in an X-ray tomograph; (b) usual picture of the capillary flow obtained from X-ray radiography. V-shape and capillary die limits are underlined by black dotted lines. Black solid lines refer to the bottom edge of the syringe. $\phi_i = \langle \Phi(y,z,0) \rangle$ where the average is taken over y and z.

apparent thinning behavior observed in cornstarch suspensions. In this situation, the sample separates into two phases: a dilute phase and a concentrated phase[13] that clogs the syringe.

To conclude this section, note that this does not preclude anisotropy or local stress heterogeneity.[22,34]

5 Measurements of the pairwise frictional profiles between particles

5.1 Experimental set-up

To measure the force profile between pairs of PVC particles, we take advantage of a quartz-tuning fork based atomic force microscope[9] (see Fig. 11a). We glue an electrochemically etched tungsten tip of approximately 50 nm end radius to a millimetric quartz tuning fork, which serves as our force sensor. Using an in-house-built nano-manipulator in a scanning electron microscope, we can glue individual PVC particles to the end of the tungsten tip. During a typical experiment, the attached particle is immersed in solvent and brought into contact with another bead, fixed on the substrate, while monitoring the force profile.

To simultaneously measure the normal and tangential force profiles between the two approaching particles, we simultaneously excite the tuning fork *via* a piezo-dither at two distinct resonance frequencies $f_N \approx 31$ kHz and $f_T \approx 17$ kHz, corresponding to the excitation of both normal (N) and shear (T)

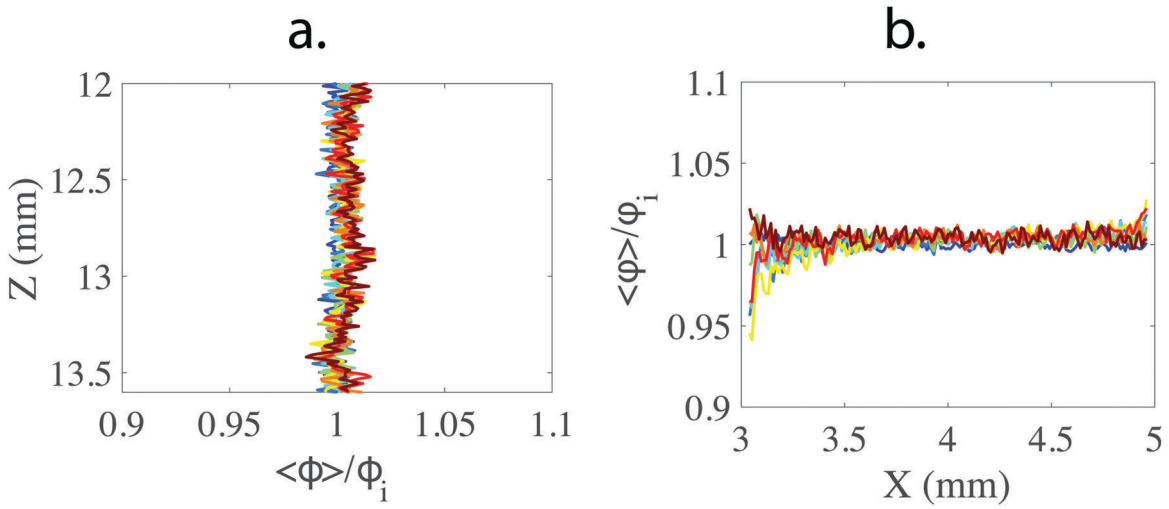

Fig. 10 Relative variation of the averaged particle volume fraction seen by the beam along (a) the flow direction Z or (b) the radial direction X for D1 60%. $\langle \phi_i \rangle$ is the value of ϕ averaged over the x direction. Applied stresses range from 180 (electric blue) to 9.8×10^3 (blue), 1.5×10^4 (cyan blue), 2.3×10^4 (green), 3.0×10^4 (yellow), 3.9×10^4 (orange), 4.6×10^4 (red), and 6.2×10^4 (brown) Pa and correspond to the ones obtained with the large PMMA syringes (from 0 to 8 bars) as shown in Fig. 5a & c (before, in and beyond the DST transition).

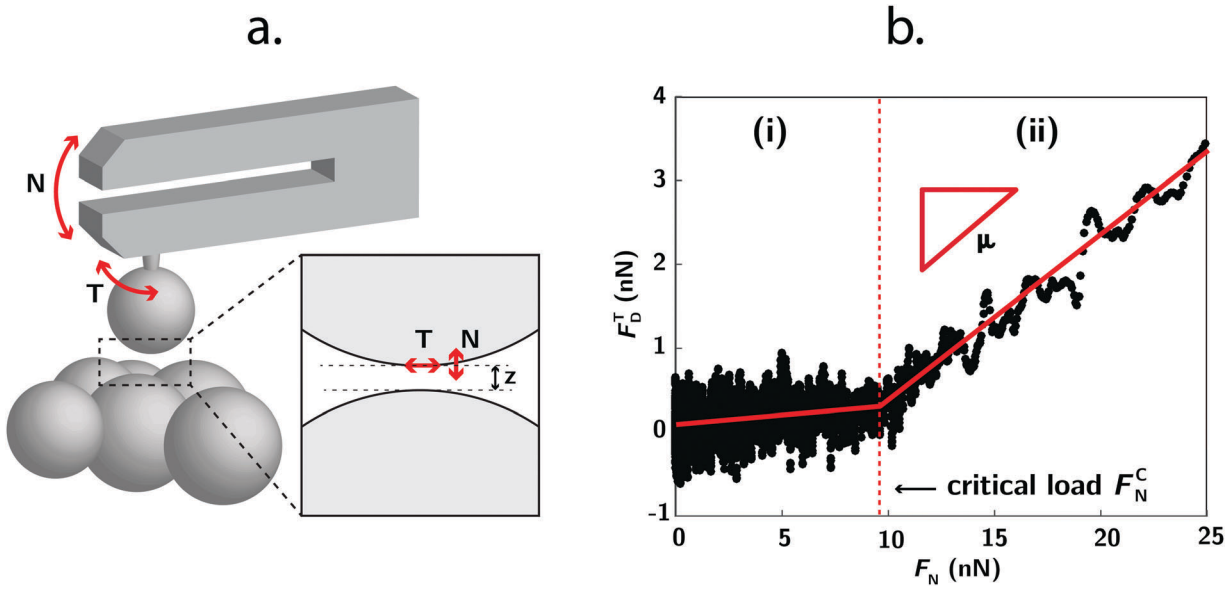

Fig. 11 (a) Sketch of the experimental set-up used to measure force and the frictional profile between the pairs of the PVC particles. A PVC particle is attached to one prong of the tuning fork and is oscillated normally (N) and tangentially (T) to a particle attached to the substrate. (b) Frictional profile between the particles of PVC 1 (tangential frictional dissipative forces F_D^T as a function of normal load F_N) showing the transition from hydrodynamic lubricated contacts (i) to frictional contacts (ii) at a critical normal load F_N^C.

modes of the tuning fork (Fig. 11a). Monitoring the changes in the resonance of each mode allows us to measure the conservative force gradient ∇F_i [N m^{-1}] and dissipative frictional forces F_D^i [N] for those two directions ($i \in \{N,T\}$).[9] In the following, we show measurements performed with particles of PVC 1. We anticipate similar friction properties for PVC 2 as surface properties are similar.

5.2 Measurements under low normal load

We have already presented in a previous work[9] the measurement of the tangential and normal dissipative and conservative forces as a function of the distance between particles. We recall in Fig. 11b, the variation of the tangential frictional dissipative force F_D^T as a function of the normal load F_N, characterizing the transition between two regimes of lubricated (i) and frictional (ii) contact at a critical normal load F_N^C. For $F_N < F_N^C$, a finite repulsive interaction between the particles exists due to entropic repulsion between polymer brushes formed at the PVC surface, and dissipative forces between particles are of hydrodynamic origin, leading to a very low friction coefficient μ. For $F_N > F_N^C$, the two particles enter into hard frictional contact, characterized by a sudden increase of dissipative tangential forces. In this second frictional regime, we recover Coulomb-type friction, with a proportionality between tangential friction and normal forces, and a friction coefficient independent of speed.[9] The transition from lubricated to frictional contacts occurs upon the application of a normal force F_N^C (or equivalently the critical pressure $P^* = F_N^C/\pi R^2$) corresponding to the load necessary to completely compress the soft polymer layers and reach hard contact. The value of this critical normal load F_N^C is a well-defined property of each particle interaction, but will also depend on the physicochemical, geometrical, mechanical and roughness surface states of the two sliding beads. Over 30 different pairs of beads,[9] we find a mean critical interaction potential $W_0 = F_N^C/(\pi R)$ equal to 6.1×10^{-3} N m^{-1} $\pm$ 2×10^{-4} N m^{-1}.

5.3 Measurements under moderate and high normal loads

We focus now on the behavior at high normal load, for which the particles experience frictional interactions. We plot in Fig. 12a the tangential dissipative friction forces F_D^T as a function of the normal load F_N, for loads up to 2 μN. Whereas in the initial frictional regime uncovered in Fig. 11b (ii), the friction was found to obey Coulomb's law,[9] we clearly observe in Fig. 12a a sublinear variation of tangential dissipative forces with normal load at larger loads. We can extract from Fig. 12a a microscopic friction coefficient defined as $\mu = F_D^T/F_N$, which we plot in Fig. 13 as a function of the normal load. μ decreases as a function of the applied load.

To understand this deviation from Coulomb's law, we express the frictional force between the two PVC surfaces as $F_D^T = \tau \cdot \mathcal{A}_{real}$, where $\mathcal{A}_{real}$ is the real area of contact, and the shear strength τ [Pa] characterizes the friction per real contact area between the PVC surfaces. The deviation from the classical Amontons–Coulomb law at large loads, *i.e.* the non-linear dependence between the tangential friction and the normal load (Fig. 12a), and the decrease in the friction coefficient μ (Fig. 13) could stem from (1) a geometrical origin, *i.e.* a non-linear variation of the real contact area $\mathcal{A}_{real}$ with the normal load F_N or (2) a physical origin, *i.e.* a decrease in the shear strength τ [Pa] with the normal load. To disentangle those two effects, we plot in Fig. 12b the tangential stiffness k_T [N m^{-1}] as a function of the normal load. k_T can be considered to be directly proportional to the real area of contact $\mathcal{A}_{real}$ (*i.e.* to the number of contacts). This tangential stiffness is found to vary proportionally to the normal load over the entire range of measurements. We thus deduce that the real area of contact

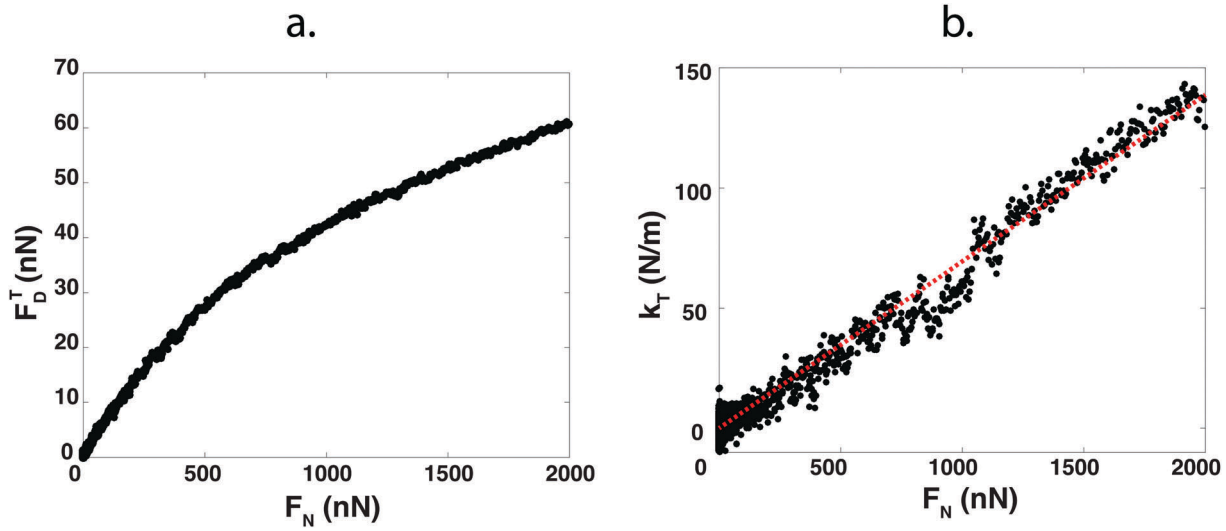

Fig. 12 (a) Tangential frictional forces F_D^T *versus* normal load F_N, showing a sublinear variation of frictional forces with normal load at large normal loads ($F_N \gg F_N^C$). The radius of the attached bead is 0.5 μm and the solvent between the two beads is pure Dinch. (b) Variation of the tangential conservative forces k_T as a function of the normal load F_N. The linear relation between k_T and F_N suggests that the real area of contact varies proportionally to the normal load.

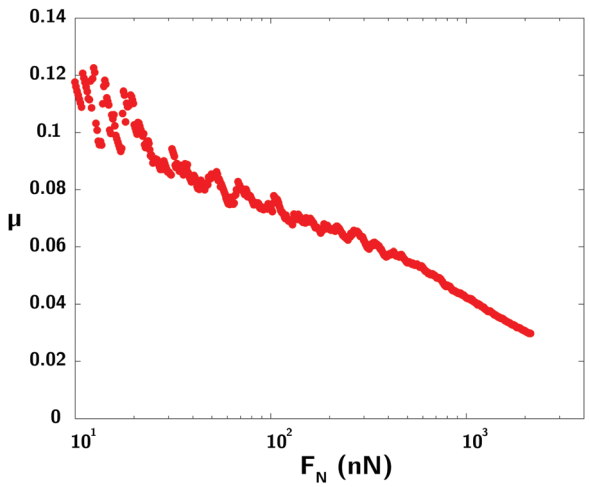

Fig. 13 Variation of the microscopic interparticle friction coefficient $\mu = F_D^T/F_N$ as a function of the normal load. μ decreases with increasing load. Note that the particles involved in this measurement are not the same as that used in Fig. 11.

increases proportionally with the normal load, in agreement with classical multi-asperity models. The non-linear variation of tangential dissipation with normal load thus has its origin in a decrease of the shear strength τ with increasing normal loads, and stems from the physical interaction between the two PVC surfaces.

Such a decrease of the friction coefficient with load has already been reported in the literature for strongly compressed polymer brushes in good solvents.[35,36] It is important to underline that the friction coefficient is a well-defined property between two particles. However, it displays a rather large distribution. Over 30 different pairs of beads, we find a mean μ coefficient under a small load equal to 0.45 ± 0.35.[9]

6 Results and discussion: toward a global vision of the viscosity of non-Brownian suspensions

Let us summarize the main points of our work. We have studied suspensions of PVC particles dispersed in a Newtonian solvent. Combining classical rotational rheometry and capillary rheometry, we point out that the viscosity of the dispersions decreases at low shear rate, increases for more than one or two orders of magnitude as a function of the applied shear for intermediate values of shear rate, and then decreases following the power law at high shear rate (Fig. 5). We show that the flow is homogeneous (Fig. 10). We observed no particle migration nor slip at the wall. In the following, we show that the presence of an additional force scale in the suspension, identified as the critical microscopic pressure $P^* = \frac{F_N^C}{\pi R^2}$ at which particles enter into contact (Fig. 11), and the non-trivial variation of the interparticle friction coefficient μ with normal load (Fig. 13) leads to a shear rate dependent rheology and allows us to rationalize the two observed shear thinning regimes.

6.1 Shear thinning at low shear rate

Let us first focus on the first regime, *i.e.* the shear thinning regime at low shear rate (Fig. 5 and 14a). In our system, this regime cannot be attributed to a competition between diffusion and convection, to the non-Newtonian properties of the solvent, nor to the migration of particles. Force measurements between the particles prove that the contact between particles is lubricated at low normal loads, *i.e.* at low shear rates (Fig. 11b). In this situation, shear thinning comes from the fact that the suspension behaves essentially as soft lubricated particles at low shear stresses, with an apparent size that includes the hard

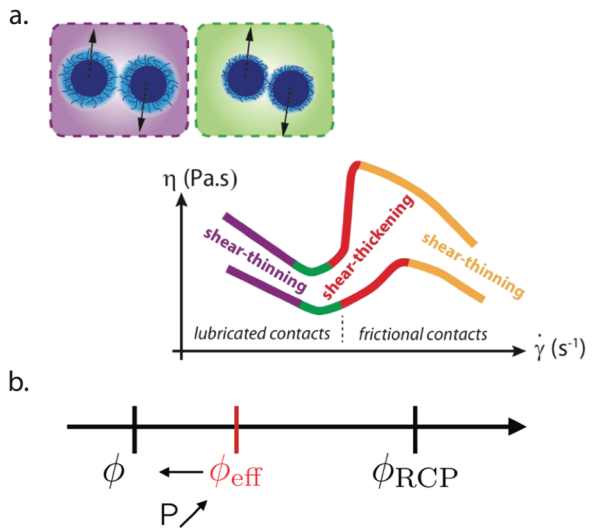

Fig. 14 (a) Scheme of the process involved in the first shear thinning regime: increasing the pressure decreases the effective size of the particles, leading to a decrease of the effective solid fraction ϕ_{eff}. (b) The decrease of the effective volume fraction ϕ_{eff} towards the solid fraction for hard spheres ϕ leads to an increase in the distance from the random close packing fraction ϕ_{RCP} at which viscosity diverges for frictionless particles, and thus a decrease of the suspension viscosity.

sphere (radius R) and a part of the surrounding soft repulsive potential, which varies as a function of shear rate. If a particle is subjected to a particular pressure P, the minimum gap $2h(P)$ between this particle and its neighbors will be such that $F_N(h) = P\pi R^2$, where F_N is the conservative normal repulsive force between the particles. Under this pressure, the apparent radius of the particle will be given by $R + h(P)$. In this regime, the particles have an apparent radius larger than that of their hard core and this effective radius decreases as a function of the applied pressure, *i.e.* applied shear rate and shear stress. As shown in Fig. 14b, the decrease of the effective radius leads to a decrease of the effective solid fraction ϕ_{eff} towards the hard sphere packing fraction ϕ. This decrease in ϕ_{eff} comes with an increase of the distance between ϕ_{eff} and ϕ_{RCP}, the random close packing fraction at which viscosity diverges for frictionless spheres, and thus to a decrease of the suspension viscosity and a shear thinning behavior. Such thinning has already been observed in a charge stabilized suspension[21,22] and predicted numerically.[23]

To go further and quantitatively analyse our results, we extract the repulsive force profiles from the rheological measurements and we compare them to the data obtained using our atomic force microscope. We start by building upon the analyses of Wyart and Cates for dense suspensions.[7] For the sake of simplicity, we assume as in ref. 7 that the pressure P and the shear stress σ are proportional, and can be expressed as

$$\sigma/\dot{\gamma} = BP/\dot{\gamma} = \eta \tag{10}$$

$$\eta = \eta_s \left(\frac{\phi_{RCP}}{\phi_{RCP} - \phi_{eff}}\right)^n \tag{11}$$

where n is a fitting parameter, η_s is the shear viscosity of the Dinch solvent, ϕ_{eff} is the effective volume fraction and ϕ_{RCP} is the random close packing fraction at which viscosity diverges for frictionless particles (see Fig. 14b). B is a constant and does not depend upon the nature of contact between particles. The effective solid fraction can be related to the apparent minimum possible gap $h(P)$ between particles and to the hard sphere volume fraction ϕ and will be given by:

$$\phi_{eff} = \phi\left(1 + \frac{h(P)}{R}\right)^3 \tag{12}$$

By combining the last two equations, we get the evolution of the interaction potential between the particles $W(h) = PR$ as a function of h.[37]

$$h = \left(\left(\frac{\phi_{eff}}{\phi}\right)^{1/3} - 1\right) \cdot R \tag{13}$$

$$\phi_{eff} = \phi_{RCP} - \left(\frac{\eta(\dot{\gamma})}{\eta(\dot{\gamma}^*)}\right)^{1/n} (\phi_{RCP} - \phi) \tag{14}$$

$$W(h) = PR = \sigma R/B = W_0(\sigma/\sigma^*) \tag{15}$$

In these expressions, $\dot{\gamma}^*$ is the shear rate at the entry of the shear thickening zone, and σ^* is the shear stress associated with the shear thickening transition. At the entry of the shear thickening zone, the particles are close to contact. This leads to $h \approx 0$ and $\phi_{eff} = \phi$. The pressure at the entry of the shear thickening zone P^* is linked to the potential of the interaction at the contact onset W_0 through $P^* = F_N^C/(\pi R^2) = W_0/R$. The knowledge of P^* allows us to also estimate B through $B = \sigma^*/P^*$. The mean value of P^* averaged over 30 measurements is equal to $P^* = 6300$ Pa, $\sigma^* = 100$ Pa and $B = 0.016$ for the D1 suspensions and to $P^* = 4200$ N, $\sigma^* = 100$ Pa and $B = 0.025$ for the D2 suspension.

To find n and ϕ_{RCP}, we measure the value of the viscosity η^* at $\dot{\gamma}^*$ where the viscosity *vs.* shear rate curve goes through a minimum as a function of the solid fraction, and fit the curve using a Krieger–Dougherty model. We get $\phi_{RCP} = 69.4\% \pm 0.25\%$ for D1 suspensions and $\phi_{RCP} = 77.2\% \pm 0.25\%$ for D2. The exponents n of the Krieger–Dougherty models are respectively $n = 2.3$ for the D1 dispersion and $n = 2.9$ for the D2 dispersion.

Fig. 15 displays the values $W(h)$ from eqn (15), which lead to the four rheological curves displayed in Fig. 5. All the data collapse on a single curve, which is very close to the repulsive profile measured by the tuning fork, shown as the black line in Fig. 15.[9] To compute this curve we use R equal to 1 μm for D1 and R equal to 1.5 μm for D2. The slight differences between the measurements and the theoretical model may be related to the polydispersity of the samples.

This quantitative analysis shows that the existence of short-ranged repulsive forces along with lubricated contacts at low particular pressure is responsible for the shear thinning behavior observed at low shear rate.

6.2 Shear thinning at high shear rate

In our system, shear thinning at high shear rate cannot be attributed to a competition between diffusion and convection,

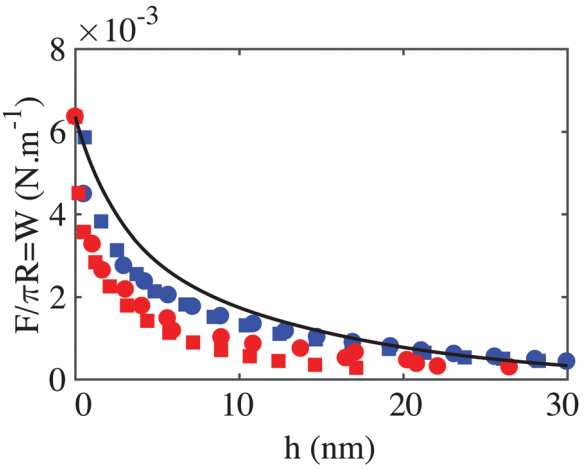

Fig. 15 Variation of the interaction potential W as a function of h. The black curve corresponds to the value of W for D1 extracted from the tuning fork experiment. The blue squares correspond to the D2 dispersion (ϕ = 0.64), the blue circles to the D2 dispersion (ϕ = 0.6), the red squares to the D1 dispersion (ϕ = 0.6) and the red circles to the D1 dispersion (ϕ = 0.55). To compute this curve, we use R equal to 1 μm for D1 and R equal to 1.5 μm for D2.

to the non-Newtonian properties of the solvent, nor to the migration of particles. Before discussing the measurements of the microscopic frictional coefficient, let us summarize the main models of the literature describing shear thinning of non-Brownian dispersions at high shear rates.

6.2.1 Analysis in the framework of the models existing in the literature. It has been proposed[11,25] that flow may deform the particles at high shear rate. The deformation δ varies as σ/G where G is the elastic modulus of the beads. The elastic modulus of PVC is equal to 3×10^9 Pa. In the shear thinning regime, the shear stress is less than 10^6 Pa. The deformation is less than 3×10^{-4} and cannot be the origin of shear thinning. The created film $h = R\delta$ due to particle deformation is thus much less than 3×10^{-10} m. Such a film is not physical since it does not contain a single molecule of Dinch.

Shear thickening relies on the transition between the lubricated contact and frictional ones. The solvent film has to be drained during the collision between the particles. At low shear rates, this process is likely to happen. However at high shear rates, one may suggest that the time required to go to the contact and drain the liquid is less than the time involved in the collision $1/\dot{\gamma}$. This would lead to fewer contacts when $\dot{\gamma}$ is increased and thus to a decrease of η with $\dot{\gamma}$. Let us estimate the time required for the particles to form the contact. By neglecting the inertial forces, the time required for the particles to go into contact may be estimated by balancing the normal dissipative forces F_d with the forces involved during the contact $PR^2 - F_{repulsive}$. $F_{repulsive}$ is the force that has to be overcome to enter into contact. Then,[9] in the shear thinning region at high shear rates, $F_{repulsive}$ is much less than PR^2. We assume P close to σ and write $F_d \simeq \frac{\eta_{solvent} R^2}{h}\frac{dh}{dt} \simeq \frac{\eta_{solvent} R^2}{\tau} \simeq \sigma R^2$. τ is the characteristic time to reach contact. We get $\tau = \frac{\eta_{solvent}}{\eta_{dispersion}}\frac{1}{\dot{\gamma}}$. In all the situations involved in the shear thinning regime, τ is much less than $1/\dot{\gamma}$, which suggests that the particles have time to come close to each other during the collision. At this stage, Dinch has to be drained from the brushes of polymers in order to obtain a frictional contact.

Mass conservation of the solvent writes $\frac{\partial c}{\partial t} = \mathrm{div}\left(kc\vec{\nabla}P\right)$, where c is the solvent fraction. During the collision, *i.e.* for a time equal to $1/\dot{\gamma}$, this leads to $\frac{\Delta c}{c} = kP/\left(a^2\dot{\gamma}\right)$. In the frictional situation, the contact has become fully plastic and deforms so that the normal stress remains quasi-constant $P = H$, where H is the hardness of the material. At room temperature, for polymer glasses, $H/E = 10^{-1}$–10^{-2}. a is the size of the micro-contact and is roughly given by $a = \sqrt{(sR_{asperity})}$, where s is the roughness of the material and $R_{asperity}$ is the radius of curvature of the asperity.

In D1 and D2 suspensions, $R_{asperity}$ is roughly equal to 100 nm and s is 2 nm, which gives a = 14 nm. k is the ratio of the permeability of the PVC brushes to Dinch over the viscosity of Dinch, $k = 10^{-20}$ kg^{-1} m^3 s. We get $\frac{\Delta c}{c} \gg 10^4$ or $10^3/\dot{\gamma}$, which proves that all the Dinch has time to drain out of the contact during the collision at least for a shear rate of less than 10^3 s^{-1}.

6.2.2 Variation of the microscopic friction coefficient. The second shear thinning behavior at large shear rates occurs after the shear thickening transition and thus happens in the context of a frictional rheology (see Fig. 16a). To explain this shear thinning behavior, we thus turn to our experimental measurements of the friction coefficient between two beads, as shown in Fig. 12 and 13. We pointed out that μ decreases as a function

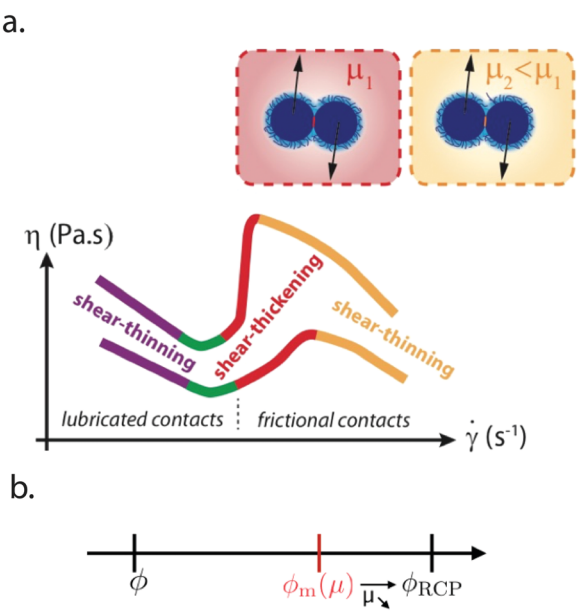

Fig. 16 (a) Scheme of the process involved in the second shear thinning regime: increasing the pressure decreases the value of the microscopic frictional coefficient μ. (b) The decrease of the microscopic friction coefficient μ leads to an increase in the critical volume fraction $\phi_m(\mu)$ at which viscosity diverges for the frictional sphere towards the random close packing fraction ϕ_{RCP}. The increasing distance between the suspension volume fraction ϕ and $\phi_m(\mu)$ with increasing pressure leads to a decrease in suspension viscosity.

of the normal load, going down from 0.12 to as low as 0.03 for normal forces up to 1 μN. In our experiments, the shear stress varies between 10^4 Pa and 10^5 Pa in the shear thinning region. Normal forces are of the order of 10^5–5×10^5 Pa with $B = 0.016$ or $B = 0.025$ (eqn (10)). Even though local heterogeneities might be present at the level of the stress field,[34] we use a simple argument to estimate the normal load. Assuming that the stress is homogeneous in the sample, the normal force applied on a single bead of radius 1 μm comprises between 0.3 and 1.5 μN, which corresponds to the range of normal loads for which μ decreases.

To go further in our analysis, we follow the model of Wyart and Cates.[7] As shown in Fig. 16b, a decrease of μ will increase the value of the friction-dependent jamming density ϕ_m and thus will increase the distance between the volume fraction ϕ and the critical volume fraction ϕ_m. It is worth noting that $\phi_m(\mu)$ is very sensitive to μ in the range 0–0.2, which corresponds to our microscopic friction coefficient variations. At the scale of the suspension, an increase in the shear rate $\dot{\gamma}$ will lead to an increase in the particular pressure and thus a decrease of the value of the inter-particle friction coefficient μ. To validate this picture, we correlate the critical volume fraction ϕ_m with the microscopic friction coefficient μ in the following.

For a frictional rheology, the viscosity of the suspension can be expressed as:

$$\eta = \eta_s \left(\frac{\phi_m(\dot{\gamma})}{\phi_m(\dot{\gamma}) - \phi} \right)^n$$

where η_s is the solvent viscosity. Here, we assume that the exponent n of the Krieger–Dougherty model does not depend upon the nature of the contact, and thus can be considered equal to the exponent found for the lubricated rheology at low shear rates (eqn (11)). This leads to $\phi_m(\dot{\gamma}) = \dfrac{\phi}{1 - \left(\dfrac{\eta_s}{\eta(\dot{\gamma})} \right)^{1/n}}$. The shear rate is given by $\dot{\gamma} = \dfrac{BF_N}{\pi R^2 \eta}$. Knowing experimentally the link between μ and F_N, we display in Fig. 17 the evolution of $\phi_m(\dot{\gamma})$ as a function of μ. The data obtained by using the rheological measurements displayed in Fig. 17 collapse on a single curve for each of the dispersions revealing the validity of our analysis. The variations of $\phi_m(\dot{\gamma})$ required to explain the shear thinning behavior are of the order of 10% when μ varies between 0.08 (close to the entry of the shear thickening zone) and 0.04–0.01 in the shear thinning zone. Such behavior is in agreement with simulations.[38]

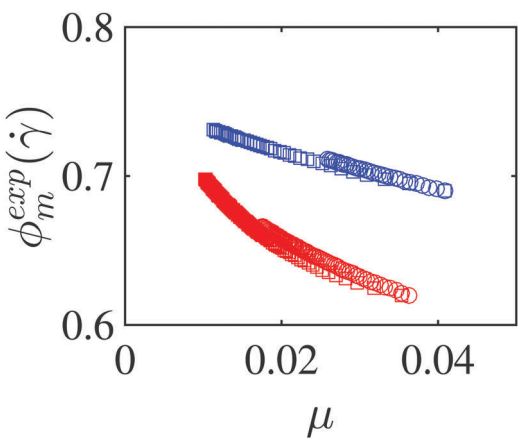

Fig. 17 Variation of $\phi_m(\dot{\gamma})$ as a function of μ. The blue squares correspond to the dispersion D2 (ϕ = 0.64), the blue circles to the D2 dispersion (ϕ = 0.6), the red squares to the D1 dispersion (ϕ = 0.6) and the red circles to the D1 dispersion (ϕ = 0.55).

7 Conclusions

We studied in this work the behavior of concentrated non-Brownian suspensions over a large range of shear rates. We evidenced two shear thinning mechanisms in those non-Brownian suspensions (Fig. 5). At low shear rate, shear thinning occurs for a lubricated rheology due to short-range repulsive forces (Fig. 14). In this regime, the suspension behaves essentially as soft particles, with an apparent size that includes the hard sphere and a part of the surrounding soft repulsive potential. An increase in the shear rate leads to an increase in the particular pressure, a decrease of the effective solid fraction and thus to a decrease of the suspension viscosity, leading to shear thinning. We have indirectly proved this mechanism by comparing the force profile extracted from the rheological data and the one measured directly. Further studies deal with the direct measurements of the hydrodynamic size of the particle by scattering.

The second shear thinning regime at high shear rate occurs after the shear thickening transition and thus for a frictional rheology (Fig. 16). At the scale of two particles, we measure a decrease of the friction coefficient at large normal loads (Fig. 13). In this second frictional regime, an increase in the shear rate leads to an increase in the particular pressure, a decrease of the inter-particle friction coefficient, and thus an increase of the critical volume fraction ϕ_m at which viscosity diverges for frictional spheres. This increase in the critical volume fraction ϕ_m with shear rate explains the observed shear thinning behavior.

In conclusion, let us evaluate the generality of our results. As pointed out in the introduction, the second shear thinning regime observed after the shear thickening transition has also been observed in cornflour suspensions. In this situation, the second shear thinning regime has been attributed to phase separation.[13] The behavior reported in this paper for PVC suspensions is thus not universal. Our ongoing work deals with experiments on silica particles stabilized by electrostatic forces. Both shear thinning regimes will be analyzed.

Conflicts of interest

There are no conflicts to declare.

Acknowledgements

The authors thank Y. Abdesselam, J. F. Agassant and R. Castellani for the measurements with the commercial capillary rheometer

in the CEMEF laboratory in Sophia-Antipolis. They also acknowledge A. Lantheaume and L. Olanier for the machining of the large volume syringe. GO thanks Solvay for financial support. AC and GO thank ANR for funding (ANR Fluididense 2017). GC thanks Tarkett for financial support.

References

1 A. Einstein, On the motion of small particles suspended in liquids at rest required by the molecular-kinetic theory of heat, *Ann. Phys.*, 1905, **17**, 549–560.
2 A. Einstein, Berichtigung zu meiner arbeit:eine neue bestimmung der moleküldimensionen, *Ann. Phys.*, 1911, **339**(3), 591–592.
3 F. Boyer, É. Guazzelli and O. Pouliquen, Unifying suspension and granular rheology, *Phys. Rev. Lett.*, 2011, **107**(18), 188301.
4 M. van Hecke, Soft matter: Running on cornflour, *Nature*, 2012, **487**(7406), 174–175.
5 E. Han, I. R. Peters and H. M. Jaeger, High-speed ultrasound imaging in dense suspensions reveals impact-activated solidification due to dynamic shear jamming, *Nat. Commun.*, 2016, **7**, 12243.
6 H. A. Barnes, Shear-thickening (''Dilatancy'') in Suspensions of Nonaggregating Solid Particles Dispersed in Newtonian Liquids, *J. Rheol.*, 1989, **33**(2), 329–366.
7 M. Wyart and M. E. Cates, Discontinuous shear thickening without inertia in dense non-brownian suspensions, *Phys. Rev. Lett.*, 2014, **112**(9), 098302.
8 R. Seto, R. Mari, J. F. Morris and M. M. Denn, Discontinuous Shear Thickening of Frictional Hard-Sphere Suspensions, *Phys. Rev. Lett.*, 2013, **111**(21), 218301.
9 J. Comtet, G. Chatté, A. Niguès, L. Bocquet, A. Siria and A. Colin, Pairwise frictional profile between particles determines discontinuous shear thickening transition in non-colloidal suspensions, *Nat. Commun.*, 2017, **8**, 15633.
10 C. Clavaud, A. Bérut, B. Metzger and Y. Forterre, Revealing the frictional transition in shear-thickening suspensions, *Proc. Natl. Acad. Sci. U. S. A.*, 2017, 201703926.
11 D. P. Kalman, *Microstructure and rheology of concentrated suspensions of near hard-sphere colloids*, PhD thesis, Delaware university, 2010.
12 A. S. Lim, S. L. Lopatnikov, N. J. Wagner and J. W. Gillespie, An experimental investigation into the kinematics of a concentrated hard-sphere colloidal suspension during Hopkinson bar evaluation at high stresses, *J. Nonnewton. Fluid Mech.*, 2010, **165**(19–20), 1342–1350.
13 A. Fall, F. Bertrand, D. Hautemayou, C. Mezière, P. Moucheront, A. Lematre and G. Ovarlez, Macroscopic Discontinuous Shear Thickening versus Local Shear Jamming in Cornstarch, *Phys. Rev. Lett.*, 2015, **114**(9), 098301.
14 E. Brown and H. M. Jaeger, Dynamic Jamming Point for Shear Thickening Suspensions, *Phys. Rev. Lett.*, 2009, **103**(8), 086001.
15 H. Lombois-Burger, P. Colombet, J. L. Halary and H. Van Damme, On the frictional contribution to the viscosity of cement and silica pastes in the presence of adsorbing and non adsorbing polymers, *Cem. Concr. Res.*, 2008, **38**(11), 1306–1314.
16 J. Qin, G. Zhang and X. Shi, Study of a Shear Thickening Fluid: The Suspensions of Monodisperse Polystyrene Microspheres in Polyethylene Glycol, *J. Dispersion Sci. Technol.*, 2017, **38**(7), 935–942.
17 R. L. Hoffman, Discontinuous and Dilatant Viscosity Behavior in Concentrated Suspensions. I. Observation of a Flow Instability, *Trans. Soc. Rheol.*, 1972, **16**(1), 155–173.
18 E. G. Barroso, F. M. Duarte, M. Couto and J. M. Maia, High strain rate rheological characterization of low viscosity fluids, *Polym. Test.*, 2010, **29**(4), 419–424.
19 N. Nakajima and E. R. Harrell, Rheology of poly(vinyl chloride) plastisol for superhigh shear-rate processing. I, *J. Appl. Polym. Sci.*, 2010, **115**(6), 3605–3609.
20 Y. Abdesselam, J.-F. Agassant, R. Castellani, R. Valette, Y. Demay, D. Gourdin and R. Peres, Rheology of plastisol formulations for coating applications, *Polym. Eng. Sci.*, 2017, **57**(9), 982–988.
21 I. M. Krieger, Rheology of monodisperse latices, *Adv. Colloid Interface Sci.*, 1972, **3**(2), 111–136.
22 B. J. Maranzano and N. J. Wagner, The effects of interparticle interactions and particle size on reversible shear thickening: Hard-sphere colloidal dispersions, *J. Rheol.*, 2001, **45**(5), 1205–1222.
23 R. Mari, R. Seto, J. F. Morris and M. M. Denn, Shear thickening, frictionless and frictional rheologies in non-brownian suspensions, *J. Rheol.*, 2014, **58**(6), 1693–1724.
24 N. Nakajima and E. R. Harrell, Rheology of PVC Plastisol at Instability Region and Beyond (Proposal for Super-High Shear-Rate Coating), *J. Elastomers Plast.*, 2009, **41**(3), 277–285.
25 D. P. Kalman, B. A. Rosen and N. J. Wagner, Effects of Particle Hardness on Shear Thickening Colloidal Suspension Rheology, *AIP Conf. Proc.*, 2008, **1027**(1), 1408–1410.
26 A. Vázquez-Quesada, R. I. Tanner and M. Ellero, Shear thinning of noncolloidal suspensions, *Phys. Rev. Lett.*, 2016, **117**(10), 108001.
27 S. J. Willey, Steady Shear Rheological Behavior of PVC Plastisols, *J. Rheol.*, 1978, **22**(5), 525–545.
28 S.-C. Dai, E. Bertevas, F. Qi and R. I. Tanner, Viscometric functions for noncolloidal sphere suspensions with newtonian matrices, *J. Rheol.*, 2013, **57**(2), 493–510.
29 E. Brown and H. M. Jaeger, The role of dilation and confining stresses in shear thickening of dense suspensions, *J. Rheol.*, 2012, **56**(4), 875–923.
30 E. B. Bagley, End Corrections in the Capillary Flow of Polyethylene, *J. Appl. Phys.*, 1957, **28**(5), 624–627.
31 B. Rabinowitsch, Uber die viskostat und elastizitat von solen, *Z. Phys. Chem., Abt. A*, 1929, **145**, 141.
32 J. R. Seth, M. Cloitre and R. T. Bonnecaze, Influence of short-range forces on wall-slip in microgel pastes, *J. Rheol.*, 2008, **52**(5), 1241–1268.

33 M. Gholami, N. Lenoir, D. Hautemayou, G. Ovarlez and S. Hormozi, Time-resolved 2D concentration maps in flowing suspensions using X-ray, *J. Rheol.*, 2017, submitted.
34 V. Rathee, D. L. Blair and J. S. Urbach, Localized stress fluctuations drive shear thickening in dense suspensions, *arXiv preprint arXiv:1702.02068*, 2017.
35 U. Raviv, R. Tadmor and J. Klein, Shear and Frictional Interactions between Adsorbed Polymer Layers in a Good Solvent, *J. Phys. Chem. B*, 2001, **105**(34), 8125–8134.
36 B. J. Briscoe and D. Tabor, The effect of pressure on the frictional properties of polymers, *Wear*, 1975, **34**(1), 29–38.
37 B. V. Derjaguin, Untersuchungen über die reibung und adhäsion, iv, *Colloid Polym. Sci.*, 1934, **69**(2), 155–164.
38 F. D. Cruz, S. Emam, M. Prochnow, J.-N. Roux and F. Chevoir, Rheophysics of dense granular materials: Discrete simulation of plane shear flows, *Phys. Rev. E: Stat., Nonlinear, Soft Matter Phys.*, 2005, **72**(2), 021309.